JOURNAL OF APPLIED PHYSICS **97**, 113523 (2005)

In situ x-ray absorption spectroscopic study of the $Li[Ni_{1/3}Co_{1/3}Mn_{1/3}]O_2$ cathode material

Aniruddha Deb[a)]
Environmental Energy Technologies Division, Lawrence Berkeley National Laboratory, One Cyclotron Road, Berkeley, California 94720

Uwe Bergmann
Stanford Synchrotron Radiation Laboratory, Sand Hill Road, Menlo Park, California 94025

Stephen P. Cramer
Physical Bioscience Division, Lawrence Berkeley National Laboratory, One Cyclotron Road, Berkeley, California 94720 and Department of Applied Sciences, University of California, Davis, California 95616

Elton J. Cairns
Environmental Energy Technologies Division, Lawrence Berkeley National Laboratory, One Cyclotron Road, Berkeley, California 94720 and Department of Chemical Engineering, University of California, Berkeley, California 94720

(Received 10 January 2005; accepted 25 March 2005; published online 1 June 2005)

The layered $LiNi_{1/3}Co_{1/3}Mn_{1/3}O_2$ system has recently drawn considerable interest for use as a cathode material for rechargeable lithium batteries. In order to investigate the charge-compensation mechanism and structural perturbations occurring in the system during cycling, *in situ* x-ray absorption spectroscopy (XAS) measurements were performed utilizing a novel electrochemical *in situ* cell specifically designed for long term x-ray experiments. The cell was cycled at a moderate rate through a typical Li-ion battery operating voltage range (2.9–4.7 V). The electrode contained 2.025 mg of $LiNi_{1/3}Co_{1/3}Mn_{1/3}O_2$ on a 25-μm Al foil and had an area of 0.79 cm^2. The x-ray absorption spectroscopy (XAS) measurements were performed at the Ni, Co, and the Mn edges at different states of charge (SOC) during cycling, revealing details about the response of the cathode to Li insertion and extraction processes. Changes of bond distance and coordination number of Ni, Co, and Mn absorbers as a function of the state of charge of the material were obtained from the extended x-ray-absorption fine structure (EXAFS) region of the spectra. The x-ray absorption near-edge structure (XANES) region was studied in order to characterize the oxidation states of the 3*d* transition metals during cycling (Li extraction/insertion). We found that oxidation states of transition metals in $LiNi_{1/3}Co_{1/3}Mn_{1/3}O_2$ are Ni^{2+}, Co^{3+}, and Mn^{4+}, whereas during charging Ni^{2+} is oxidized to Ni^{4+} through an intermediate stage of Ni^{3+}, Co^{3+} is oxidized almost to Co^{4+} and, utilizing Faraday's calculation and XAS results, the Co was found to be at $Co^{3.92+}$ at the end of the charge, while Mn was found to be electrochemically inactive and remains as Mn^{4+}. The EXAFS data that were collected continuously during cycling revealed details about the response of the cathode to Li insertion and extraction. These measurements on the $LiNi_{1/3}Co_{1/3}Mn_{1/3}O_2$ cathode confirmed that the material retains its symmetry and good structural short-range order leading to superior cycling. © *2005 American Institute of Physics*. [DOI: 10.1063/1.1921328]

I. INTRODUCTION

The search for environmentally friendly and cost-effective lithium battery electrode materials with higher capacity and high cycling stability is an ongoing quest. With the emergence of portable telecommunications, computer equipment, and ultimately hybrid electric vehicles, there has been a great demand for substantial improvement in energy storage devices which can lead to less expensive batteries with longer lifetime and smaller size and weight.[1] Over the past years there has been a growing interest in lithium insertion materials, largely because they potentially have a wide range of application for positive and/or negative electrodes in lithium-ion batteries. Lithium transition-metal oxides have always attracted attention as candidate electrode materials for lithium-ion batteries. Among them, layered $LiTO_2$ (T = 3*d* transition metal element) materials with an α-$NaFeO_2$ structure have been widely investigated.[2] The current commercial lithium-ion battery is based on a layered oxide, $LiCoO_2$ cathode[3] (space group *R*3*m*), with a theoretical capacity of 274 mAh/g, good reversibility, and charge/discharge rate capability. However, the practically attainable capacity is found to be only 120–130 mAh/g in the voltage range of 2.8–4.2 V,[4,5] and due to the high cost of Co there has been a considerable interest in developing cathode materials based on Mn, Ni, or V as lower-cost alternatives. An improved operational capacity can be achieved by utilizing Li_yNiO_2 and its doped derivatives.[6] But these materials are

[a)]Author to whom correspondence should be addressed; FAX: 510-486-7303; electronic mail: ADeb@lbl.gov

found to possess unstable cycling performance, and their capacity fades especially when charged and discharged at high rates. The poor rate capability and instability associated with these materials is ascribed to Ni migration into sites within the depleted Li layer for $y \leqslant 0.5$, which causes a deleterious change in the cathode structure.[7] In the last few years, Co has been investigated as a substitution metal in the $LiNi_{1-x}Co_xO_2$ system, mainly to improve the stability of the cathode by creating a more stable $LiNiO_2$–$LiCoO_2$ solid solution.[8] Layered $LiMnO_2$ and its Co derivatives $Li(Mn_{1-x}Co_x)O_2$ ($x \leqslant 0.5$), which are isostructural with $LiNiO_2$, have also been investigated. The cathodic capacity for this system was found to be high (180–200 mAh/g), but, unfortunately, the main concern on cycling of this material has been capacity fading and conversion to the spinel structure.[9] Moreover, a layered system $LiNi_{0.8}Co_{0.2}O_2$ has attracted attention as a new cathode material in lithium-ion batteries for hybrid electric vehicle applications.[10] Compared to $LiCoO_2$, this system proved to possess enhanced electrochemical performance at a projected lower cost. The electrochemical performance of the layered system $Li(Ni_{1/2}Mn_{1/2})O_2$ was reported by Lu *et al.*[11] and by Ohzuku and Makimura.[12] While the former study observed a reversible capacity of 160 mAh/g (in the range of 2.0–4.6 V), the latter group observed a reversible capacity of 150 mAh/g (range of 2.5–4.3 V). Furthermore, a stable cycling behavior has been observed for the solid solution $xLi(Ni_{1/2}Mn_{1/2})O_2 \cdot (1-x)Li_2TiO_3$, $x=0.95$,[13] but as $Li(Ni_{1/2}Mn_{1/2})O_2$ can be derived from the solid solution $Li(Ni_xLi_{(1/3-2x/3)}Mn_{(2/3-x/3)})O_2$, $x=1/2$, Mn and Ni were assigned to be in the 4+ and 2+ oxidation state by Lu *et al.*,[11] and the electrochemical processes involved $Ni^{2+} \rightarrow Ni^{4+}$ with two-electron transfer, in agreement with the obtained capacity and the stoichiometry of the compound.

In recent years there has been an upsurge in the search for technologically important new layered materials such as $LiNi_{1/3}Co_{1/3}Mn_{1/3}O_2$. This system has been of significant interest and has been intriguing, as the Mn was found to be electrochemically inactive. One study suggests that the material possesses a capacity of 150 mAh/g in the range of 2.5–4.2 V,[12] while another study reports a capacity of 200 mAh/g (in the range of 2.5–4.6 V at 0.17 mA/cm^2).[14] This system can be considered as a special instance of Co substitution in the parent compound $Li(Ni_{1/2}Mn_{1/2})O_2$,[15] with a chemical composition of $Li(Ni_xCo_{1-2x}Mn_x)O_2$, where $x=1/3$. The reason for its improved electrochemical performance is still being investigated. Hence, x-ray absorption spectroscopy *in situ* experiments during cycling will be of immense importance and will be informative in developing a complete understanding of the charge-discharge mechanism in this system. There have been numerous efforts to observe the detailed changes that occur in and on the electrodes during the charging and discharging processes. In the case of modern Li-ion batteries the electrode materials permit lithiation and delithiation, a mechanism that, in the long run, can result in severe degradation of the electrodes, strongly limiting the life time of the battery. Real-time tracking of the changes in the electrode materials undergoing electrochemical reactions is best performed by utilizing an *in situ* electrochemical cell. The advantage of *in situ* XAS measurements lies in the ability to directly monitor detailed structural changes in the electrode material as ion extraction/insertion proceeds. This, along with the simultaneous electrochemical measurements, provides unique valuable information about the relationship between structure and electrochemical properties, which is not accessible from *ex situ* experimental measurements.

Here, we apply transmission x-ray absorption spectroscopy to investigate $LiNi_{1/3}Co_{1/3}Mn_{1/3}O_2$ electrodes (as used in Li-ion batteries) in various states of charge (SOC). XAS offers the possibility to follow the structural and electronic changes *in situ* during an ongoing electrochemical process. Information about the valence state of the investigated element (in our case, Mn, Co, and Ni) and its electronic configuration was obtained from the XANES region of the K-absorption edge, whereas the EXAFS region was used to probe the structure around the x-ray absorbing atom. Very recently, *ex situ* work on characterization and analysis of $LiNi_{1/3}Co_{1/3}Mn_{1/3}O_2$ has been performed using an x-ray diffraction technique (XRD), but to the best of our knowledge there has been no *in situ* EXAFS investigation reported on this system. It is important to mention that in contrast to XRD, which gives one a good picture of the long-range structural changes in the cathode, *in situ* XAS investigations during cycling can be illuminating in their own right, providing an understanding of the oxidation state as well as short-range ordering and providing a baseline for further studies in which the electrode material is modified by the introduction of additional elements. In addition, XAS can distinguish between the bulk properties (measurement in transmission mode) and surface properties (by fluorescence, or even more restricted to surface by electron yield or grazing incidence measurements). In this paper, we present a comprehensive analysis of Ni, Co, and Mn K-edge EXAFS, as well as an analysis of the *X*-ray absorption near-edge structure (XANES).

II. EXPERIMENTAL PROCEDURES

A. $LiNi_{1/3}Co_{1/3}Mn_{1/3}O_2$ electrode and electrochemical XAS cell assembly

The experiments were performed with a complete $Li/LiNi_{1/3}Co_{1/3}Mn_{1/3}O_2$ cell. The prepared layered compound was single phase, as was verified by x-ray diffraction (XRD). Electrodes were fabricated from an intimate mixture of the $LiNi_{1/3}Co_{1/3}Mn_{1/3}O_2$ powder that comprised 85% by weight of the total electrode with 8% polyvinylidene difluoride polymer binder (Kynar) and 7% compressed acetylene black in N-methyl-2-pyrrolidonone (NMP). The black viscous slurry consisting of $LiNi_{1/3}Co_{1/3}Mn_{1/3}O_2$, acetylene black, and Kynar was cast onto an aluminum foil of thickness 25 μm by the doctor blade technique.[16] Then the NMP was evaporated at 120 °C for about 1 h, and finally the electrodes were dried under vacuum at 150 °C for 16 h. An electrode with a 10-mm diameter was punched from the electrode foil sheet. The thickness of the active mass on the electrode was about 200 μm and the charge density was about 0.69 mAh/cm^2. The electrochemical *in situ* XAS cell is shown in Fig. 1. For a complete detailed electrochemical

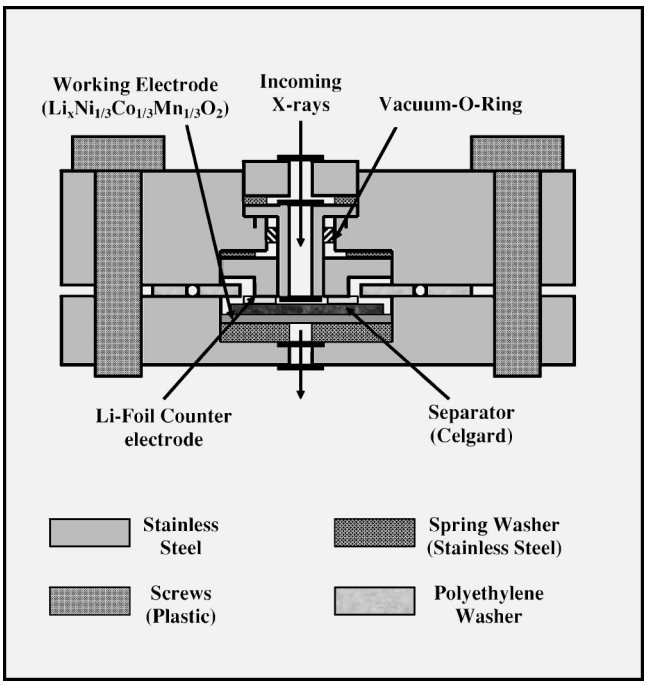

FIG. 1. Schematic view of electrochemical *in situ* XAS cell.

XAS cell design and assembly the reader is referred to Deb *et al.*[17] A sheet of porous polypropylene membrane (from Celgard, Celgard 3400) was used as a separator. The separator was punched with an outer diameter of 10 mm and an inner diameter of 4 mm. Then all necessary cell parts, chemicals, and tools for the assembly were placed in an argon-filled glove box in the laboratory. The separator was placed on top of the working electrode ($LiNi_{1/3}Co_{1/3}Mn_{1/3}O_2$) (Fig. 1), where the separator was soaked with electrolyte 1-M $LiPF_6$ dissolved in 50 wt % ethylene carbonate (EC) and 50 wt % dimethylcarbonate (DMC) obtained as a solution from Merck Company. Finally, to complete the cell assembly a piece of lithium foil counter electrode was then punched with an outer diameter of 10 mm and an inner diameter of 6 mm from fresh supplies and placed on top of the separator. A computer-controlled Princeton Applied Research Model VERSA potentiostat/galvanostat was used for cycling the electrochemical cell under a constant current control.

The electrochemical cycling (charge and discharge) of the cell was performed at a constant current density of 0.14 mA/cm^2 between 2.9 and 4.7 V, which corresponds to about the 5-h rate. The *in situ* measurements performed during the charging and discharging were carried out at various states of charge of the electrode. The spectra presented here were obtained during the charging process at the 0% SOC, 25% SOC, 40% SOC, 75% SOC, 90% SOC, and finally 100% SOC (corresponding to 4.7 V versus Li).

For the measurements using the model compounds, the samples were diluted with boron nitride (BN), and 0.78-cm^2 pellets were then pressed using a pressure of 9 tons, yielding pellets of 400-μm thickness. Finally, the pellets were mounted on aluminium sample holders using Kapton adhesive foil on both sides of the sample.

B. X-ray absorption spectroscopy measurement and data analysis

The XAS measurements were performed on the bending magnet beamline station D of the DuPont-Northwestern-Dow Collaborative Access Team (DND-CAT) at the Advanced Photon Source, Argonne National Laboratory. A water-cooled Si(111) double-crystal monochromator was used, and the energy resolution of the monochromatic beam was determined to be ~1.0 eV. Transmission ion chambers were used to measure the incident (I_0), transmitted (I_t), and reference (I_{ref}) signals. The I_0 and the I_t chambers were filled with a helium-nitrogen mixture (10/90% and 11/89%, respectively), while the I_{ref} chamber was filled with a nitrogen-argon mixture (82/18%). A beam size of 0.3×0.5 mm was chosen in order for the beam to pass easily through the *in situ* cell x-ray window resulting in an incident photon flux of $\sim10^{11}$ photons per second. The monochromator was scanned in energy from 200 eV below to 800 eV above the Mn and Ni K-absorption edges (6539 and 8333 eV), whereas the data range collected at the Co K-absorption edge was limited to 8250 eV (12.7 $Å^{-1}$) by the onset of the Ni K edge. Data were collected within this energy range, with a step size of 0.2 eV in the respective edge region. The energy calibrations at each edge were performed using Mn, Co, and Ni metal foils between the I_t and I_{ref} ion chambers, respectively. XAS spectra were collected at each of these absorption edges.

Extended x-ray-absorption fine structure (EXAFS) data reduction was performed using the EXAFSPAK software package[18] and ATHENA.[19] The resulting $\chi(k)$ function was then weighted with k^3 to account for the damping of oscillations with increasing k. The radial structure functions were obtained by Fourier transformation of $k^3\chi(k)$ using a k range of 1.0–16.2 $Å^{-1}$ for Mn and Ni and 1.0–12.7 $Å^{-1}$ for Co.

III. RESULTS AND DISCUSSION

A. Structure of $LiNi_{1/3}Co_{1/3}Mn_{1/3}O_2$

The structure of $LiNi_{1/3}Co_{1/3}Mn_{1/3}O_2$ has been previously investigated and reported by different groups.[20,13] Our XRD investigation of the $LiNi_{1/3}Co_{1/3}Mn_{1/3}O_2$ electrode revealed a typical XRD pattern similar to that of $LiCoO_2$, as reported earlier by Yabuuchi and Ohzuku.[20] The atomic structure fits the space-group symmetry of $R3m$ (α-$NaFeO_2$ type), ITC #166 (International Tables for X-Ray Crystallography). The structure has Li ions at the 3*a* sites, the transition metal ions (M=Mn, Co, and Ni) at the 3*b* sites, and O ions at the 6*c* sites in a hexagonal setting. However, it is important to note that a partial interchange of occupancy of Li and transition metal (M) ions among the sites (i.e., Li in 3*b* and M in 3*a* sites) leads to a disordering in the structure called "cation mixing,"[21,22] which leads to the deterioration of the electrochemical performance of this layered compound. Recently, Koyama *et al.*[23] investigated this layered compound by first-principle calculations using a superlattice model, where they found the average Mn–O, Co–O, and Ni–O distances to be 1.94 Å, 1.92 Å, and 2.02 Å, respectively. In contrast to the large decrease in the unit-cell volume for $LiCoO_2$ (about 6%), $LiNiO_2$ (about 10%), and $LiMnO_2$ (about 8%) during delithiation (i.e., during charging or oxi-

dation), $LiNi_{1/3}Co_{1/3}Mn_{1/3}O_2$ exhibits a small change in the cell volume (about 3%), proving to be beneficial with regard to cycling stability, cell life, and rate capability.

B. XAS results for $LiNi_{1/3}Co_{1/3}Mn_{1/3}O_2$

1. XANES

Unlike $LiNiO_2$ (Ref. 24) and $LiCoO_2$,[25] $Li_xNi_{1/3}Co_{1/3}Mn_{1/3}O_2$ has a hexagonally layered structure, and there has been no phase change to a secondary phase with monoclinic symmetry when Li is extracted from its lattice. This has been verified by *ex situ* XRD measurements performed on electrochemical cells.[26] For $Li_{1-x}Ni_{1/3}Co_{1/3}Mn_{1/3}O_2$ it is now proposed that an extraction of Li ions results in the lattice shrinkage along the *a* and *b* directions while an expansion takes place along the *c* direction. Moreover, it has also been hypothesized that the driving force for monoclinic distortion is not the Jahn–Teller effect of Ni^{3+}, but a lithium vacancy ordering that leads to a super structure in $LiNiO_2$.[25] Conversely, as $Li_{1-x}Ni_{1/3}Co_{1/3}Mn_{1/3}O_2$ does not exhibit any phase change to monoclinic symmetry, it possesses a good ability to cycle Li into and out of the Li layer while maintaining its hexagonal ($R3m$) symmetry. In general, the shape of the K-edge XANES of the transition metal oxides provides unique information about the site symmetry and the nature of bonding with surrounding ligands, while the threshold energy position of the absorption edge provides information about the oxidation state of the probed atom. Figure 2 shows the x-ray absorption near-edge structure (XANES) regions at 0% SOC compared to model compounds at the Mn, Co, and Ni edges, respectively. The qualitative difference is immediately apparent from the figures. In Fig. 2(a) the Mn K-edge XANES spectrum of $LiNi_{1/3}Co_{1/3}Mn_{1/3}O_2$, when compared with model compounds Mn_2O_3 (Mn^{3+}) and MnO_2 (Mn^{4+}), reveals that the edge energy is identical to that of MnO_2 (Mn^{4+}), indicating that the oxidation state of Mn in $LiNi_{1/3}Co_{1/3}Mn_{1/3}O_2$ is tetravalent (Mn^{4+}). The XANES spectrum for the sample at the Co K edge was compared with that of $LiCoO_2$, as shown in Fig. 2(b). The comparison clearly indicates that the XANES spectrum for the Co K edge of the sample is identical to that of $LiCoO_2$ (Co^{3+}). Thus, Co in $LiNi_{1/3}Co_{1/3}Mn_{1/3}O_2$ can be considered as Co^{3+}. The XANES spectrum for the sample at the Ni K edge was compared with that for Nickel (II) oxide [$NiO(Ni^{2+})$] and with layered $LiNi_{0.8}Co_{0.2}O_2$ (Ni^{3+}), as shown in Fig. 2(c). The XANES spectrum for the Ni K edge of the sample is similar to that of Nickel (II) oxide, indicating that Ni in $LiNi_{1/3}Co_{1/3}Mn_{1/3}O_2$ is divalent [Ni^{2+}] at 0% SOC, whereas the Ni K-edge XANES is similar to that of layered $LiNi_{0.8}Co_{0.2}O_2$ at 40% SOC, confirming that Ni in $LiNi_{1/3}Co_{1/3}Mn_{1/3}O_2$ is trivalent [Ni^{3+}] at 40% SOC.

Figure 3 shows XANES spectra for selected SOC values at the Mn, Co, and Ni edges, respectively. For Mn K-edge XANES [Fig. 3(a)] during charging the edge position of the first five scans at different charge states did not exhibit any significant edge shift to higher energies, suggesting that the Mn oxidation state remains unchanged, i.e., the Mn^{4+} atom is electrochemically inactive. However, during charging, the XANES observed for the Co K edge [Fig. 3(b)] shows a

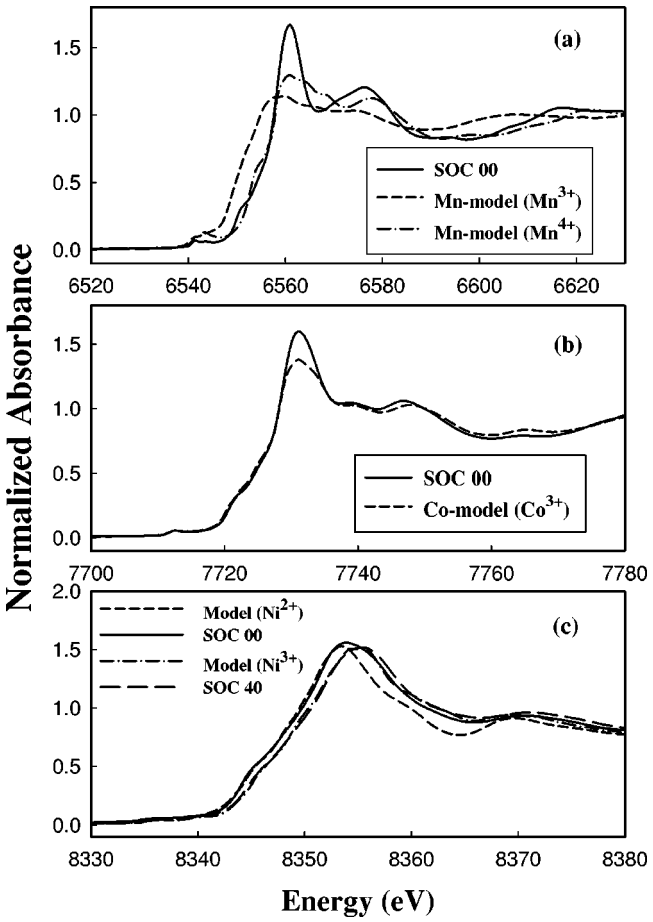

FIG. 2. Calibrated and normalized XANES comparison of (a) Mn K edge for $LiNi_{1/3}Co_{1/3}Mn_{1/3}O_2$, observed at 0% SOC with the model compound Mn_2O_3 (Mn^{3+}) (broken line) and MnO_2 (Mn^{4+}) (dash-dot line); (b) Co K edge for $LiNi_{1/3}Co_{1/3}Mn_{1/3}O_2$, observed at 0% SOC with the model compound $LiCoO_2$ (Co^{3+}); and (c) Ni K edge for $LiNi_{1/3}Co_{1/3}Mn_{1/3}O_2$, observed at 0% SOC (thick solid line) and 40% SOC (thick broken line) with the model compounds Nickel (II) oxide (Ni^{2+}) (broken line) and $LiNi_{0.8}Co_{0.2}O_2$ (Ni^{3+}) (dash-dot line), respectively.

progression of the entire pattern from lower energy to higher energy as a function of the decreased Li content (at the five different charge states), indicating the oxidation of Co^{3+} towards Co^{4+} (almost Co^{4+} as it will be shown in the following section). The results for the XANES spectra for the Ni K edge are shown in Fig. 3(c), at the five different charge states. From here it is seen that the Ni K edge shows two stages during charging. The first stage is from 0% SOC to 40% SOC and the second stage is from 40% SOC to 75% SOC. Above 75% SOC, the XANES spectrum of the Ni K edge did not move noticeably to a higher energy. This two-stage observation may be attributed to the two-electron reaction of the Ni ions (Ni^{2+}/Ni^{3+} and Ni^{3+}/Ni^{4+}) during charging. It is important to mention here that similar observations have recently been reported by Koyama *et al.*,[23] using *ab initio* calculations, that the redox reaction in $Li_{1-x}Ni_{1/3}Co_{1/3}Mn_{1/3}O_2$ consists of Ni^{2+}/Ni^{3+}, Ni^{3+}/Ni^{4+}, and Co^{3+}/Co^{4+}, respectively. However, in their work they predicted the above redox reaction for the ranges of $0 \leqslant x \leqslant 1/3$, $1/3 \leqslant x \leqslant 2/3$, and $2/3 \leqslant x \leqslant 1$, respectively. Thus our experimental observation has been consistent with these calculations, except the range for the Co^{3+}/Co^{4+} redox reac-

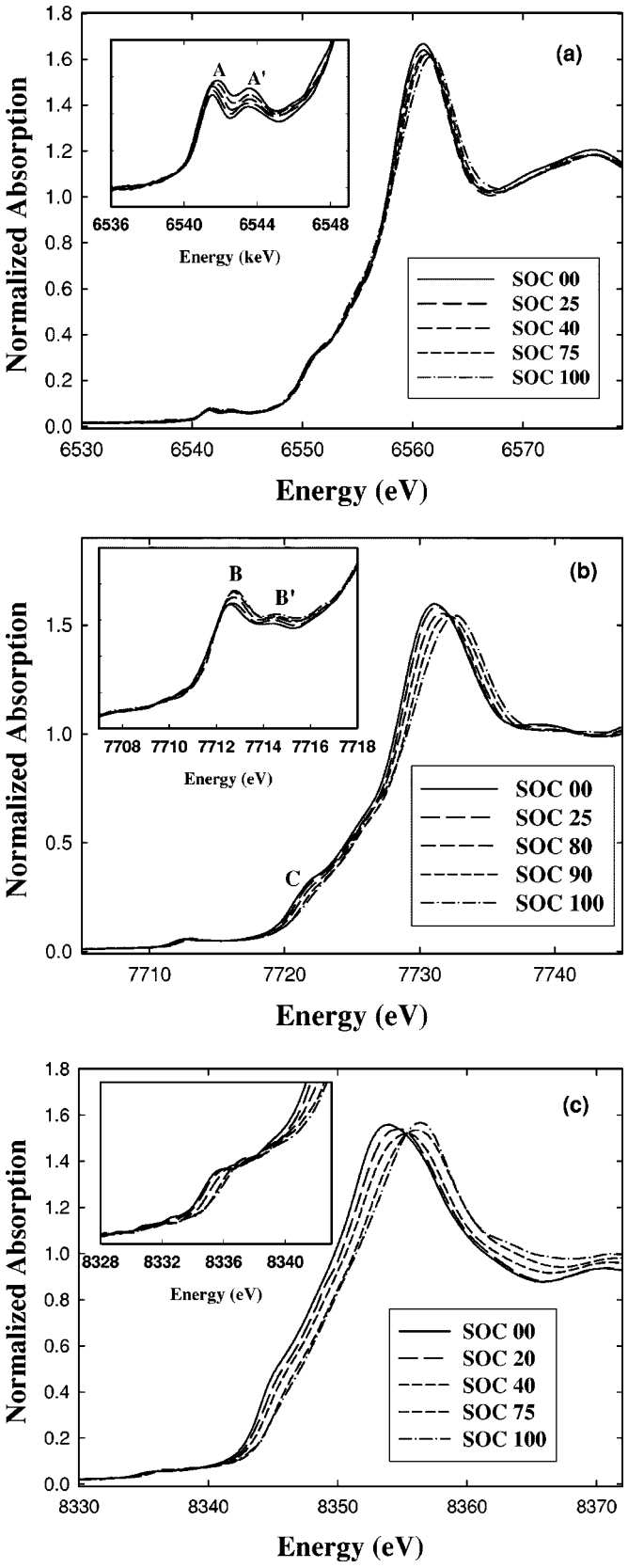

FIG. 3. Calibrated and normalized XANES spectra for $Li_{1-x}Ni_{1/3}Co_{1/3}Mn_{1/3}O_2$ at different states of charge at the (a) Mn K edge (0% SOC, 25% SOC, 40% SOC, 75% SOC, and 100% SOC); (b) Co K edge (0% SOC, 25% SOC, 80% SOC, 90% SOC, and 100% SOC); and (c) Ni K edge (0% SOC, 20% SOC, 40% SOC, 75% SOC, and 100% SOC), respectively. The insets show the nature of the preedge peaks of the respective XAS spectra.

tion, which they proposed to take place for $2/3 \leqslant x \leqslant 1$, while our experimental observation indicates that the Co^{3+}/Co^{4+} oxidation reaction occurs for essentially the entire range of x in the sample. This small discrepancy can be attributed to the fact that the calculations were performed assuming an equilibrium homogeneous state, while, actually, the particles are in a nonequilibrium heterogeneous state. During discharge, these processes are reversed electrochemically: Li is inserted in the lattice structure, the Co^{4+} and Ni^{4+} are reduced to Co^{3+} (trivalent) and Ni^{2+} (divalent) states, and the M(metal)–O and M–M bond lengths return to their original values. Hence only the data during the charging cycle have been presented here.

The insets of Figs. 3(a), 3(b), and 3(c) show the nature of the preedge region of the respective XAS spectra. The preedge results provide additional information about the nature of the electronic states. For many transition elements, the preedge peaks occur well below the main edge ($\sim$15 eV below) and are assigned to transitions to empty states with d-like character, i.e., these are $1s$ to $3d^{(n+1)}$ transitions[27,28] where n is the initial number of d electrons and $(n+1)$ includes the excited electron in the final state, which usually includes the effect of a core hole. The $1s \rightarrow 3d$ transitions are directly allowed through a very weak quadrupole transition[29] or allowed via an admixture of $3d$ and $4p$ states.[30] In the preedge region for Mn [Fig. 3(a), inset], all the spectra recorded during delithiation show two peaks denoted by A and A' (near 6541 and 6543 eV), which are assigned as the transitions from the core $1s$ level to unoccupied $3d$ states which are, in turn, electric dipole forbidden. Experimentally, the quadrupole nature of the $1s \rightarrow 3d$ preedge feature in $D_{4h}CuCl_4^{2-}$ was demonstrated by Hahn *et al.*[30] with an analysis of the angular dependence of the $1s \rightarrow 3d$ transition intensity using polarized synchrotron radiation and oriented single crystals. The p-orbital mixing into $3d$ orbitals can also contribute to the preedge intensity, which has much higher intensity than the electric quadrupole-allowed transition. Thus, even though this transition is dipole forbidden, the preedge peaks here could be discerned due to quadrupole-allowed transitions and/or due to the mixing of the $4p$ and $3d$ states. The weak intensity of the preedge is indicative of the octahedral coordination as opposed to the tetrahedral coordination from which strong preedge intensity is found.[31] The position and the shape of these preedge peaks are now well known to be closely related to the oxidation state of the absorbing ion and the local arrangement of backscattering ions, respectively. It is also evident here that the two peaks (A and A') at the preedge region are discernible because the manganese is in the tetravalent state, as a preedge with only one peak characteristic feature is observed for trivalent manganese compounds. The latter characteristic single-peak preedge feature for trivalent manganese compounds can be interpreted as a result of the splitting of the t_{2g} and e_g energy levels modified by Jahn–Teller deformation as shown earlier by Horne *et al.*[32] The preedge features observed in the Co XANES spectra [Fig. 3(b), inset], are due to Co $1s \rightarrow 3d$ transitions, and are not well structured, but it clearly shows two edges with some weak indication of an energy splitting in between. The preedge features (B and B') are assigned

here to the $1s \rightarrow t_{2g}$ and $1s \rightarrow e_g$ transitions. The energy difference between Co t_{2g} and Co e_g orbitals in octahedral oxygen-coordinated compounds is found to be about 2.5 eV,[33] which corresponds to the separation of the t_{2g} and e_g transitions. It is important to note that the presence of the two transitions indicates at least a partial high-spin configuration. Here, the preedge features are not clearly split; this may indicate delocalized electrons in the band structure or an overlapping mixture of low-spin $^1A_1(t_{2g}^6 e_g^0)$, intermediate $^3T_1(t_{2g}^5 e_g^1)$, and high-spin $^5T_3(t_{2g}^4 e_g^2)$ states. Transitions from $1s$ to the t_{2g} orbitals are both symmetry and dipole forbidden, but they do occur, albeit very weakly, due to the mixing with the oxygen p orbitals and quadrupole transitions. Transitions from $1s$ to e_g orbitals are also dipole forbidden, and hence also much weaker than the symmetry- and dipole-allowed $1s \rightarrow 4p$ main transition. We also observe a shoulder (C) at about 7221 eV, which corresponds to the shake-down process in which $1s \rightarrow 4p$ transition with ligand $\rightarrow 3d$ electron transition or ligand to metal charge transfer (LMCT) occurs $[1s^1c3d^6 \rightarrow 1s^1c3d^7L]$, as observed for $Dy_{1-x}Ca_xCoO_3$ (Ref. 34) or for $La_{1-x}SrCoO_3$,[35] where it was shown that the LMCT state $t_{2g}^6 e_g^1 L^1$ contributes about 45% to the ground state. Since the binding energy decreases due to the core-hole screening effect in Co by an electron transferred in ligand, the transition in the shake-down process occurs at a lower energy.[36] For Ni, as shown in Fig. 3(c) (inset), the preedge is almost absent. In octahedral Ni (II) complexes only the $1s \rightarrow 3d$ transition is allowed; and furthermore, this $1s \rightarrow 3d$ transition is symmetry forbidden for centrosymmetric pointgroups.[37] This means that highly symmetrical octahedral complexes will not show any prepeaks, while nonsymmetrical octahedral complexes can be detected by their higher $1s \rightarrow 3d$ peak intensity. Hence the intensity of the $1s \rightarrow 3d$ peak can be used as an indicator of the geometry in octahedral complexes. In Fig. 3(c) the absence of a $1s \rightarrow 3d$-transition preedge leads to the conclusion that the local environment of the Ni atoms is highly symmetrical. It is important to mention here that any distortion of the octahedral environment would remove the center of inversion symmetry, and a preedge or a shoulder in the XANES spectra is expected.[38] As evidenced from Fig. 3(c), the XANES spectra observed during the different states of charge during cycling (delithiation or oxidation) show the absence of a preedge which again strengthens the conclusion that the local octahedral environment of the Ni atoms remains highly symmetrical during the charging process.

In order to present a quantitative picture of how the oxidation process is taking place in this system, we have shown here Fig. 4, which depicts the plot of the white line peak position as a function of the SOC as opposed to the edge position, defined by the energy at half of the edge step for the Co, and the Ni K edge, observed during delithiation (charge) and lithiation (discharge). Here, we have included also the data of scans that have been taken in between the SOC values reported (A, B, C, D, and E). For the Co and the Ni metal centers, the change in the peak position has been about +1.91 and +3.0 eV, respectively, as the lithium content changes from the OCV (open circuit voltage) fully discharged state to the fully charged (4.7 V versus Li) state. From the figure it is

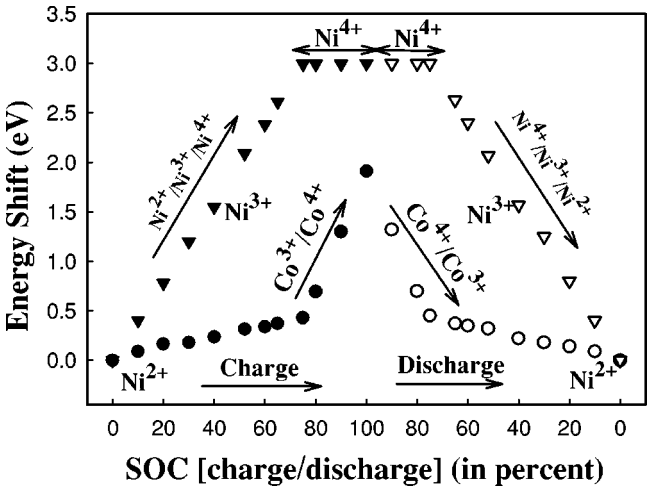

FIG. 4. Plot of the white line energy shift vs the state of charge (SOC) for Co and Ni K edge. The filled symbols (● and ▲) represent the data during charging (i.e., during delithiation), while the empty symbols (○ and △) represent the data during discharging (i.e., during lithiation).

evident that for the Co edge the oxidation state is changing smoothly and nearly proportionally to the SOC [except after 75% SOC where there is an increase in slope (Fig. 4) which is consistent with our Faraday's law calculation (Fig. 5)], while for the Ni edge the situation is not very clear, but the quantitative and qualitative indicators show that the oxidation consists of two stages (from 0% SOC to 40% SOC and from 40% SOC to 75% SOC). This is due to the two-electron reaction of Ni ions as discussed earlier. After 75% SOC the Ni edge does not change significantly, suggesting that Ni^{2+} is fully oxidized to Ni^{4+}, while charge compensation still occurs in Co (Fig. 4). To obtain a further qualitative and quantitative picture about the valence change during the charging process (with respect to the capacity change) of the constituent transition metals in this compound, we here tried to combine the XAS and the electrochemistry information using Faraday's law. Using Faraday's law the theoretical capacity

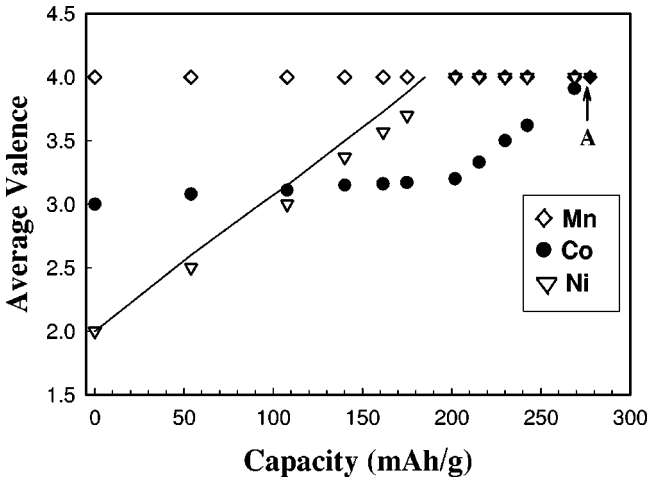

FIG. 5. Average valence vs capacity profiles for the first charge of the cell for the transition metals Ni (▽), Co (●), and Mn (◇). The average valence of Ni (▼) and that of Mn (◆) at the theoretical calculated capacity (278 mAh/g) have been shown here as position A. The solid line is the guide using Faraday's law if all the charge is used for changing the nickel valence from Ni^{2+} to Ni^{4+}.

of $LiNi_{1/3}Co_{1/3}Mn_{1/3}O_2$ is 277.68 mAh/g. So, theoretically, for the average valence change of one for the transition metals (Ni^{2+} to N^{3+}, Ni^{3+} to Ni^{4+}, and Co^{3+} to Co^{4+}) in this compound, the capacity used will be a third of the total theoretical capacity, i.e., 92.56 mAh/g. Hence using the experimentally measured capacity at each state of the charging process, along with the average valence change from the XAS results (Fig. 4) and the theoretical capacity, we can represent the average Ni and Co valence as

$$\mathrm{Ni_{val}(average)} = 2.0 + \left[\frac{\text{Expt. measured capacity(mAh/g)}}{92.56\ \text{mAh/g}}\right] \times (\mathrm{Ni_{frac}}), \quad (1)$$

$$\mathrm{Co_{val}(average)} = 3.0 + \left[\frac{\text{Expt. measured capacity(mAh/g)}}{92.56\ \text{mAh/g}}\right] \times (\mathrm{Co_{frac}}), \quad (2)$$

and

$$\mathrm{Ni_{frac}} + \mathrm{Co_{frac}} = 1, \quad (3)$$

where Ni_{frac} is the fraction of the charge that causes change in the Ni valence and Co_{frac} is the fraction of the charge that causes change in the Co valence.

From the XAS results it is observed that Ni^{2+} changes to Ni^{3+} at 40% SOC (108 mAh/g) and finally changes to Ni^{4+} at 75% SOC (202 mAh/g). Hence taking the Ni valence information and the measured capacity (mAh/g) at different states of charge in Eq. (1), we can find the Ni_{frac}. Then, using this information in Eq. (3) we can find the Co average valence at different SOC. This quantitative information is shown in Fig. 5, where we can see that during the first charge cycle the Co is almost changed from Co^{3+} to Co^{4+}. In Fig. 5 we have shown that at the theoretical capacity of 277.68 mAh/g, Mn is Mn^{4+} and Ni is Ni^{4+}, while we found that at the measured extraction capacity of the first cycle (269 mAh/g) Mn is Mn^{4+}, Ni is Ni^{4+}, and Co is $Co^{3.92+}$. In Fig. 5 the line shows the guidance from Faraday's law on how the Ni valence changes if all of the charge is used to change the Ni valence only. The observed increase in slope of the Co K-edge white line in Fig. 4 after 75% SOC can now be explained by the Faraday's law results in Fig. 5. This increase in slope is due to the fact that after 75% SOC Ni is at Ni^{4+}, and the whole of the charge is now used to change the valence of Co, as can be seen from Fig. 5.

2. EXAFS *during the charging cycle*

The local structure of the Mn, Co, and Ni ions in $Li_xMn_{1/3}Co_{1/3}Ni_{1/3}O_2$ was measured by EXAFS. The backgrounds were subtracted by extrapolating a Victoreen-type function from the preedge region, and EXAFS oscillations $\chi(k)$ were extracted using cubic spline baseline functions.[39] The radial structure functions for the central absorbing Mn, Co, and Ni atoms were obtained by Fourier transformations of the EXAFS oscillations. Fourier transformations were performed over the k range as mentioned in Sec. II B using k^3 weighting (Kaiser–Bessel window). In all cases the Li contribution to XAFS was ignored because of the low backscattering ability of the lithium. Figure 6 shows the normalized $k^3\chi(k)$ function for selected scans at different SOC values during the charging cycle, as a function of $k(\text{Å}^{-1})$ for Mn, Co, and Ni. It can be seen that the data quality is very good at the Mn, Co, and Ni edges. The peak intensity and broadness of the radial structure function correlate to the coordination number (CN) and Debye–Waller factors (σ) which reflect the thermal fluctuations and/or local order.[40] Only small changes take place in the case of Co and Ni between the different SOC values. This can be more clearly understood from the results of the FT (Fourier Transform) of the data at selected SOC's, as shown in Figs. 7, 8, and 9. It should be noted that the Ni EXAFS extends to a k value of $\sim$15 Å^{-1}, but the Co EXAFS extends to only $\sim$12.5 Å^{-1}. The lower range of the Co EXAFS is due to the presence of the Ni edge at 8.33 keV. The first peak at $\sim$1.9 Å in Figs. 7, 8, and 9 is due to the Mn–O, Co–O, and Ni–O interaction, respectively. During charging (or delithiation) it is seen that the Mn–O distance remains nearly unchanged, contrary to the gradual dwindling of the Co–O distances and the decrease of the Ni–O distances. These variations of the interatomic distances are closely related or can be attributed to the change in the valence state in the transition metals. In the presence of an octahedral crystal field, the d orbitals split into triply degenerate (t_{2g}) and a higher-energy doubly degenerate set (e_g). Hence the outermost electronic configuration of Co^{3+}/Co^{4+} can be represented as $t_{2g}^6e_g^0/t_{2g}^5e_g^0$, while for Ni^{2+}/Ni^{4+} (or Ni^{3+}/Ni^{4+}), it can be represented as $t_{2g}^6e_g^2/t_{2g}^6e_g^0$ (or $t_{2g}^6e_g^1/t_{2g}^6e_g^0$). Thus during the oxidation reaction of the charging cycle, the change in energy in Co^{3+}/Co^{4+} is very

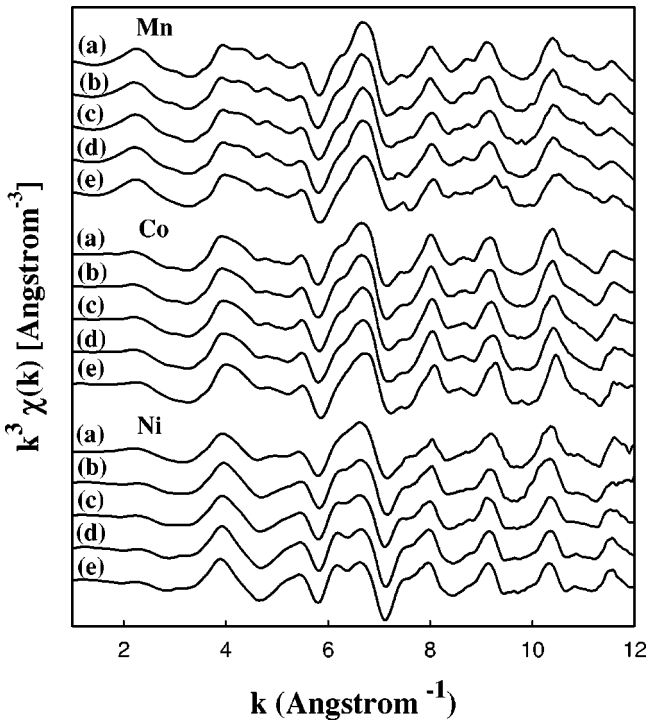

FIG. 6. Selected $k^3\chi(k)$ data observed for Mn at (a) 0% SOC, (b) 25% SOC, (c) 40% SOC, (d) 75% SOC, and (e) 100% SOC; for Co at (a) 0% SOC, (b) 25% SOC, (c) 80% SOC, (d) 90% SOC, and (e) 100% SOC; and for Ni K edges at (a) 0% SOC, (b) 20% SOC, (c) 40% SOC, (d) 75% SOC, and (e) 100% SOC.

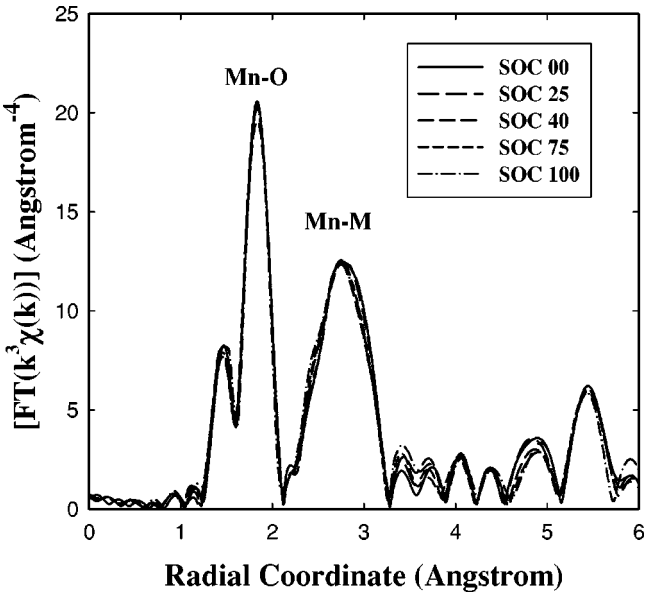

FIG. 7. Magnitude of the k^3-weighted Fourier transform of $Li_{1-x}Ni_{1/3}Co_{1/3}Mn_{1/3}O_2$ at the Mn K edge at selected SOC during the charge cycle (k range=1.5–15.1 Å). M represents the transition metal atom.

small because the change takes place only in the t_{2g} degenerate set, which results in a very small change in the ionic radius ($R^{3+}_{Co} \sim 0.54$ Å/$R^{4+}_{Co} \sim 0.53$ Å), whereas the variation in energy for Ni^{2+}/Ni^{4+} (or Ni^{3+}/Ni^{4+}), where the change takes place between the lower t_{2g} and higher e_g sets, would be larger, inducing a larger change in the ionic radius ($R^{2+}_{Ni} \sim 0.69$ Å/$R^{3+}_{Ni} \sim 0.56$ Å/$R^{4+}_{Ni} \sim 0.48$ Å). It can be seen that for 0% SOC, the amplitude of the Ni–O peak is lower than that of the Co–O peak. Also, unlike $Li_{1-x}Ni_{0.5}Co_{0.5}O_2$ (Ref. 41 and $Li_{1-x}NiO_2$,[42] here as the sample is delithiated it can be seen that the amplitude of the Ni–O and the Co–O peaks almost remains the same. These observations can be best understood by considering the local structure of Ni and Co in

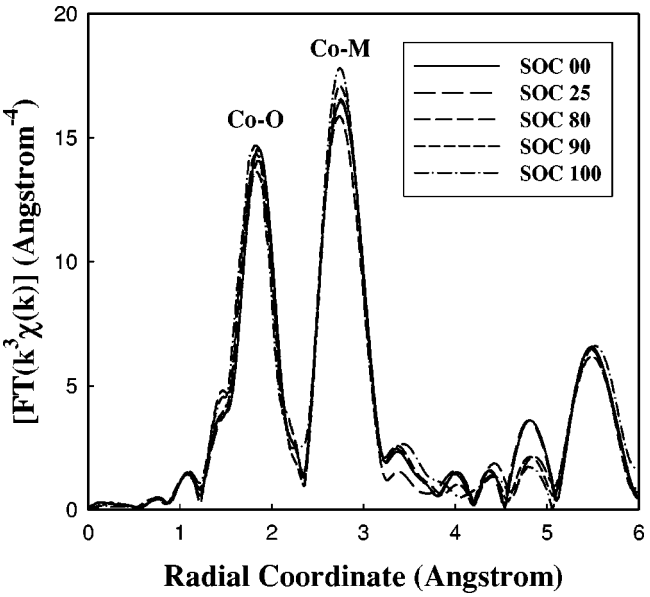

FIG. 8. Magnitude of the k^3-weighted Fourier transform of $Li_{1-x}Ni_{1/3}Co_{1/3}Mn_{1/3}O_2$ at the Co K edge at selected SOC during the charge cycle (k range=1.5–12.5 Å). M represents the transition metal atom.

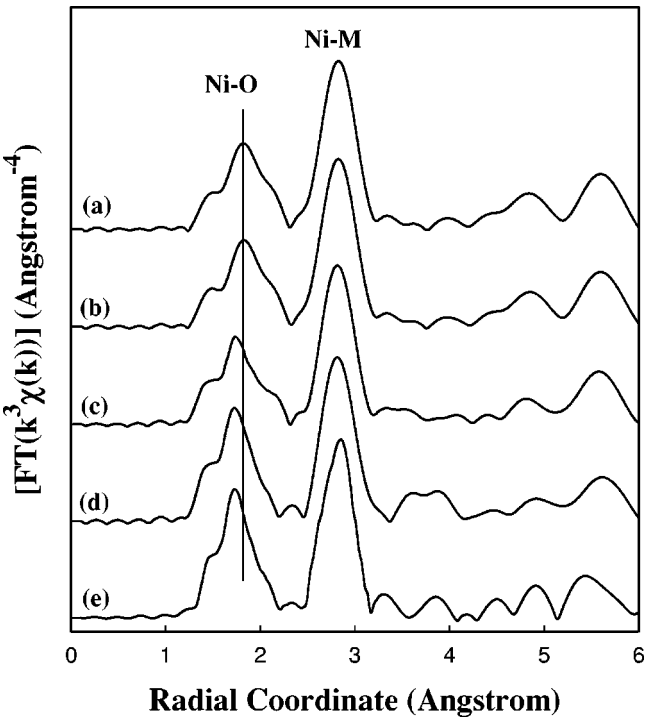

FIG. 9. Magnitude of the k^3-weighted Fourier transform of $Li_{1-x}Ni_{1/3}Co_{1/3}Mn_{1/3}O_2$ at the Ni K edge at selected SOC during the charge cycle (k range=1.5–15.1 Å). The labels (a), (b), (c), (d), and (e) represent the FT observed at the 0%, 20%, 40%, 75%, and 100% SOC, respectively. M represents the transition metal atom.

pure $LiNiO_2$ and $LiCoO_2$. As observed earlier, in $LiNiO_2$ (Ref. 43) oxygen atoms are present at two different distances surrounding Ni. This distorted octahedral coordination is consistent with a Jahn–Teller effect expected for Ni^{3+} in a low-spin state. For the $Li_{1-x}NiO_2$ system during delithiation the increase of the Ni–O peak amplitude has been ascribed to the changes in the local structure of the Ni created by the oxidation of the Ni^{3+} to Ni^{4+}. Since Ni^{4+} is not a Jahn–Teller active ion, the oxidation of Ni^{3+} to Ni^{4+} results in a diminution of the Jahn–Teller effect which results in an increased amplitude of the Ni–O peak. In contrast to the $LiNiO_2$ system, the $Li_{1-x}CoO_2$ system during delithiation does not exhibit any increase of the Co–O peak, which has been ascribed to the absence of the Jahn–Teller effect in the case of Co^{3+}. Thus based on these observations, it is understood that the absence of a Jahn–Teller active ion (i.e., Co^{3+} and Ni^{2+} are not Jahn–Teller active ions) in this system results in a similar amplitude of the Ni–O and the Co–O interaction in the FT of $Li_{1-x}Ni_{1/3}Co_{1/3}Mn_{1/3}O_2$ during delithiation.

The second peak at ~2.8 Å in Figs. 7, 8, and 9 corresponds to a metal–metal interaction. It can be seen that at the Co and the Ni edges the peak position shifts to lower R values as Li is deintercalated. In pure $LiNiO_2$ (Ref. 41) a similar behavior was observed by Nakai and Nakagome for the Ni–Ni interaction. In contrast, in pure $LiCoO_2$ the peak representing the Co–Co interaction does not shift upon delithiation.[44] They also observed that the peak amplitude of the Co–Co interaction reduces as Li is deintercalated. The small shift in peak position of the Co-metal interaction as well as the increase in amplitude of the peak in delithiation

TABLE I. Structural parameters from nonlinear least-squares fits to the first two peaks of the Fourier transform at the Mn K edge at different states of charge (SOC). The SOC (in percent), shell (Z_a–Z_b), coordination number (CN), bond distance (R), and Debye–Waller disorder (σ^2) are tabulated. The coordination number (CN) of both Mn–O and Mn–M contributions were constrained to be six. The number in the parentheses is the uncertainty in the last digit or digits of the parameter.

SOC (%)	Z_a–Z_b	CN	R(Å)	$\sigma^2(A^2\ 10^{-3})$
00	Mn–O	6	1.910(8)	2.7(5)
	Mn–M	6	2.885(9)	3.3(3)
25	Mn–O	6	1.908(8)	2.9(4)
	Mn–M	6	2.857(9)	3.1(4)
40	Mn–O	6	1.904(6)	2.9(6)
	Mn–M	6	2.842(9)	3.0(5)
75	Mn–O	6	1.899(7)	3.1(5)
	Mn–M	6	2.838(9)	3.2(4)
100	Mn–O	6	1.900(5)	3.1(4)
	Mn–M	6	2.841(9)	3.2(5)

TABLE III. Structural parameters from nonlinear least-squares fits to the first two peaks of the Fourier transform at the Ni K edge at different states of charge (SOC). The SOC (in percent), shell (Z_a–Z_b), coordination number (CN), bond distance (R), and Debye–Waller disorder (σ^2) are tabulated. The coordination number (CN) of both Ni–O and Ni–M contributions were constrained to be six. The number in the parentheses is the uncertainty in the last digit or digits of the parameter.

SOC (%)	Z_a–Z_b	CN	R(Å)	$\sigma^2(A^2\ 10^{-3})$
00	Ni–O	6	1.945(9)	4.1(4)
	Ni–M	6	2.868(8)	4.8(6)
20	Ni–O	6	1.921(8)	4.3(3)
	Ni–M	6	2.844(5)	4.8(7)
40	Ni–O	6	1.902(8)	4.3(5)
	Ni–M	6	2.831(8)	4.9(6)
75	Ni–O	6	1.872(7)	4.6(4)
	Ni–M	6	2.826(6)	4.8(5)
100	Ni–O	6	1.870(7)	4.5(5)
	Ni–M	6	2.829(8)	4.7(6)

in $Li_{1-x}Ni_{1/3}Co_{1/3}Mn_{1/3}O_2$ show clearly that Co is not present as isolated $LiCoO_2$-like entities but may be present as a substitutional entity for Ni-type sites in the host lattice. A quantitative analysis to obtain EXAFS structural parameters of Mn, Co, and Ni absorbers was performed based on a two-shell model, obtained by nonlinear least-squares fits to the first two peaks of the FT spectra at the K edges of Mn, Co, and Ni, respectively, in $Li_{1-x}Ni_{1/3}Co_{1/3}Mn_{1/3}O_2$. The bond distances ($R$) and the Debye–Waller factors (σ) were left as free parameters, and the coordination number (CN) of Mn–O, Co–O, Ni–O, Mn–M, Co–M, and Ni–M was kept fixed to the crystallographic value of six. The structural parameters obtained by curve fitting are summarized in Tables I, II, and III. The first shell metal–oxygen (Mn–O, Co–O, and Ni–O) interaction distances at various charge and discharge states are shown in Fig. 10. It is evident from the figure that the Mn–O distances varied the least (at the most by 0.01 Å), while the Co–O distances varied by about 0.05 Å and the Ni–O distances varied the most by about 0.08 Å. It is important to note here that we observe for Ni–O distances above 75% state of charge, the change in the distance is negligible and is <0.002 Å; this is consistent with the fact that after 75% SOC in the system the Ni^{2+} is changed fully to Ni^{4+} (as also evidenced from Fig. 4). The observation of the significant decrease in the Ni–O bond distance can be explained by the oxidation of Ni^{2+} to Ni^{4+} since the ionic radius of Ni^{2+} (0.69 Å) is larger than that of Ni^{4+} (0.46 Å).[45] The Ni^{4+}–O bond distance in this material ($\sim$1.87 Å) is consistent with other previously reported Ni^{4+}–O bond distances observed in compounds such as $BaNiO_3$ and $KNiIO_6$($\sim$1.88 Å).[46,47] This also indicates that at the end of the charge Ni^{2+} is completely oxidized to Ni^{4+}. Finally, the second shell metal–metal (Mn–M, Co–M, and Ni–M) interaction distances at various charge and discharge states are shown in Fig. 11. It is interesting to note here that the changes in M–M distances at the Mn, Co, and Ni K edges between the initial and the fully charged state varies at the most by 0.05 Å (0.04 Å for Mn–M, 0.05 Å for Co–M, and

TABLE II. Structural parameters from nonlinear least-squares fits to the first two peaks of the Fourier transform at the Co K edge at different states of charge (SOC). The SOC (in percent), shell (Z_a–Z_b), coordination number (CN), bond distance (R), and Debye–Waller disorder (σ^2) are tabulated. The coordination number (CN) of both Co–O and Co–M contributions were constrained to be six. The number in the parentheses is the uncertainty in the last digit or digits of the parameter.

SOC (%)	Z_a–Z_b	CN	R(Å)	$\sigma^2(A^2\ 10^{-3})$
00	Co–O	6	1.932(7)	3.0(4)
	Co–M	6	2.852(8)	3.7(3)
25	Co–O	6	1.929(7)	2.9(3)
	Co–M	6	2.829(8)	3.3(2)
80	Co–O	6	1.911(3)	3.0(4)
	Co–M	6	2.814(8)	3.4(5)
90	Co–O	6	1.893(5)	3.2(3)
	Co–M	6	2.815(8)	3.6(4)
100	Co–O	6	1.882(5)	3.4(4)
	Co–M	6	2.816(8)	3.6(5)

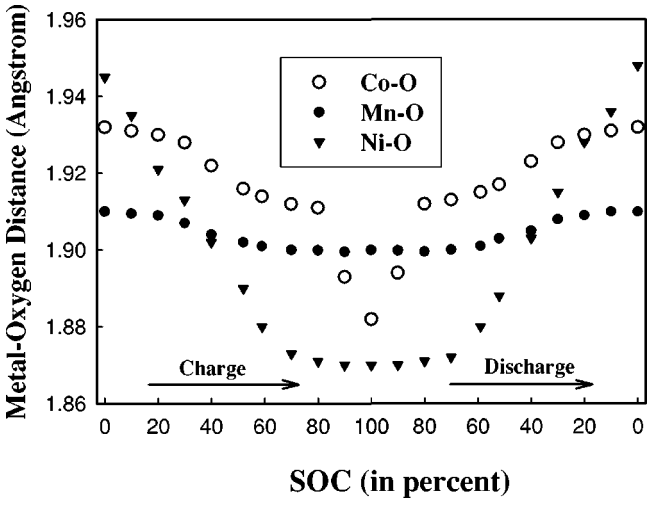

FIG. 10. First shell metal–oxygen bond length changes during $Li/Li_xNi_{1/3}Co_{1/3}Mn_{1/3}O_2$ cell cycling. The filled symbols (● and ▼) represent the Mn–O and Ni–O bond distances, while the empty symbol (◯) represents the Co–O bond distances as observed during different states of charge and discharge.

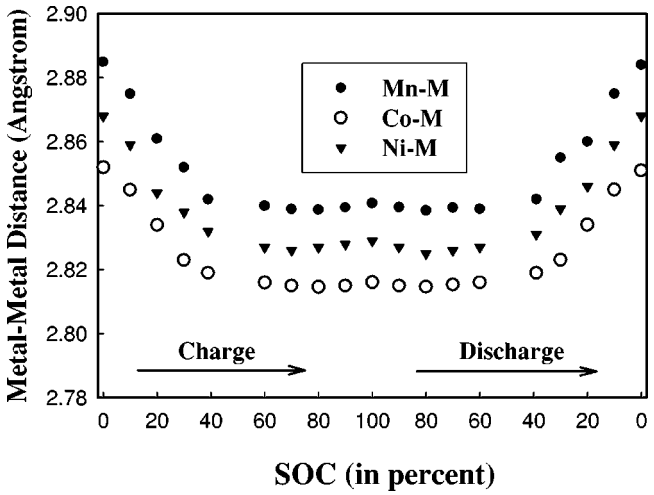

FIG. 11. Second shell metal–metal bond length changes during $Li/Li_xNi_{1/3}Co_{1/3}Mn_{1/3}O_2$ cell cycling. The filled symbols (● and ▼) represent the Mn–*M* and Ni–*M* bond distances, while the empty symbol (◯) represents the Co–*M* bond distances as observed during different states of charge and discharge.

0.055 Å for Ni–*M*)—about 1.6% contraction. It is seen from Fig. 11 that on delithiation the bond distances (Ni–*M*, Co–*M*, and Mn–*M*) decrease upon charging but tend to increase slightly at the end of the charge. These metal–metal distances correspond to the *a* lattice parameter of the trigonal *R*3*m* cell. The changes observed here in the metal–metal distances are consistent with the changes seen in the case of x-ray diffraction pattern of $Li_xNi_{1/3}Co_{1/3}Mn_{1/3}O_2$.[48]

IV. CONCLUSIONS

An XAS characterization of $Li_xNi_{1/3}Co_{1/3}Mn_{1/3}O_2$-based electrode material during charging and discharging cycles has been performed using an *in situ* electrochemical cell. The XAFS has provided us with an excellent tool for analyzing the changes that occur when Li is cycled into and out of the layered lattice of $Li_xNi_{1/3}Co_{1/3}Mn_{1/3}O_2$ in a Li-ion battery. The XANES results confirm that during the charging of $Li_xNi_{1/3}Co_{1/3}Mn_{1/3}O_2$ to 4.7 V the oxidation state of manganese does not change and remains tetravalent $[Mn^{4+}]$ until the end of charging and was found to be electrochemically inactive, whereas divalent nickel $[Ni^{2+}]$ is oxidized to tetravalent nickel $[Ni^{4+}]$ through an intermediate stage of trivalent nickel $[Ni^{3+}]$, and finally cobalt is found to be oxidized from Co^{3+} to almost Co^{4+} during the entire range of the state of charge as seen from the Faraday's law results. The small volumetric changes and the retention of the hexagonal structure confirm that this material possesses very desirable characteristics for an electrode, which makes it an excellent choice for Li-ion cell applications. When all the Ni atoms are oxidized to Ni^{4+}, the Ni atoms are coordinated by six oxygen atoms at ~1.87 Å. This Ni–O bond distance is consistent with what is expected for a Ni^{4+}–O bond. The EXAFS data show that the change in the R_{M-O} from the initial to the fully charged state varies by $\leqslant$0.08 Å, while the change in the R_{M-M} from the initial to the fully charged state varies by $\leqslant$0.06 Å, confirming that only minor changes occur in the structure of the electrode during electrochemical cycling.

ACKNOWLEDGMENTS

We acknowledge Dr. M. Doeff of the Materials Science Division, Lawrence Berkeley National Laboratory for supplying us with the $LiNi_{1/3}Co_{1/3}Mn_{1/3}O_2$ electrodes. We also acknowledge Dr. C. S. Johnson of the Chemical Engineering Division, Argonne National Laboratory for allowing us to use a glove box for assembling our electrochemical cell. This work was supported by the director of the Office of Basic Energy Sciences, Chemical Sciences Division of the U.S. Department of Energy under Contract No. DE-AC03-76SF00098. Work was performed at the DND-CAT beamline which is supported by the E. I. DuPont de Nemours and Co., the Dow Chemical Company, the U.S. National Science Foundation through Grant No. DMR-9304725, and the State of Illinois through the Department of Commerce and the Board of Higher Education Grant No. IBHE HECA NWU 96. SSRL is operated by Stanford University on behalf of the U.S. Department of Energy, Office of Basic Energy Science.

[1] A. G. Ritchie, J. Power Sources **96**, 1 (2001).
[2] R. Koksbang, J. Barker, H. Shi, and M. Y. Saidi, Solid State Ionics **84**, 1 (1996).
[3] P. G. Bruce, Chem. Commun. (Cambridge) **18**, 17 (1997).
[4] J. Fan and P. S. Fedkiw, J. Power Sources **72**, 165 (1998).
[5] A. Manthiram and J. Kim, Chem. Mater. **10**, 2895 (1998).
[6] C. Delmas *et al.*, Electrochim. Acta **45**, 243 (1999).
[7] T. Ohzuku, A. Ueda, and M. Nagayama, J. Electrochem. Soc. **140**, 1862 (1993).
[8] C. Delmas, I. Saadoune, and A. Rougier, J. Power Sources **43**, 595 (1993).
[9] A. R. Amstrong, R. Gitzendanner, A. D. Robertson, and P. G. Bruce, Chem. Commun. (Cambridge) **1**, 1833 (1998); A. R. Amstrong, A. D. Robertson, R. Gitzendanner, and P. G. Bruce, J. Solid State Chem. **145**, 549 (1999).
[10] X. Zang *et al.*, J. Electrochem. Soc. **148**, A463 (2001).
[11] Z. Lu, D. D. MacNeil, and J. R. Dahn, Electrochem. Solid-State Lett. **4**, A191 (2001); Z. Lu and J. R. Dahn, J. Electrochem. Soc. **149**, A815 (2002).
[12] T. Ohzuku and Y. Makimura, Chem. Lett. **30**, 642 (2001).
[13] J.-S. Kim, C. S. Johnson, and M. M. Thackeray, Electrochem. Commun. **4**, 205 (2002).
[14] N. Yabuuchi and T. Ohzuku, Extended abstract, *11th International Meeting on Lithium Batteries (IMLB 11), Monterey, CA, 23–28 June 2002* (unpublished).
[15] Z. Lu, D. D. MacNeil, and J. R. Dahn, Electrochem. Solid-State Lett. **4**, A200 (2001); D. D. MacNeil, Z. Lu, and J. R. Dahn, J. Electrochem. Soc. **149**, A1332 (2002).
[16] K. M. Shaju, G. V. Subba Rao, and B. V. R. Chowdari, Solid State Ionics **148**, 343 (2002).
[17] A. Deb, U. Bergmann, E. J. Cairns, and S. P. Cramer, J. Synchrotron Radiat. **11**, 497 (2004).
[18] G. N. Goerge and I. J. Pickering, EXAFSPAK: A suite of computer programs for analysis of x-ray absorption spectra, Stanford Synchrotron Radiation Laboratory (SSRL), California, 1993.
[19] M. Newville, J. Synchrotron Radiat. **8**, 322 (2001).
[20] N. Yabuuchi and T. Ohzuku, J. Power Sources **119–121**, 171 (2003).
[21] Y. Gao, M. V. Yakovleva, and W. B. Ebner, Electrochem. Solid-State Lett. **1**, 117 (1998).
[22] J. R. Mueller-Neuhaus, R. A. Dunlap, and J. R. Dahn, J. Electrochem. Soc. **147**, 3598 (2000).
[23] Y. Koyama, I. Tanaka, H. Adachi, Y. Makimura, and T. Ohzuku, J. Power Sources **119–121**, 644 (2003).
[24] I. Saadoune and C. Delmas, J. Solid State Chem. **136**, 8 (1998).
[25] T. Ohzuku and A. Ueda, J. Electrochem. Soc. **141**, 2972 (1994).
[26] D.-C. Li, T. Muta, L.-Q. Zhang, M. Yoshio, and H. Noguchi, J. Power Sources **132**, 150 (2004).
[27] J. S. Griffith, *The Theory of Transition Metal Ions* (Cambridge University Press, Cambridge, England, 1961).
[28] S. Sugano, Y. Tanabe, and H. Kamimura, *Multiplets of Transition-Metal*

Ions (Academic, New York, 1970), Vol. 1, p. 73.
[29]A. Manceau, A. I. Gorshkov, and V. A. Drits, Am. Mineral. **77**, 1133 (1992); B. Poumellec, V. Kraizman, Y. Aifa, R. Cortes, A. Novakovich, and R. Vedrinskii, Phys. Rev. B **58**, 6133 (1998); O. Sipr, A. Simunek, S. Bocharov, T. Kirchner, and G. Drager, Phys. Rev. B **60**, 14115 (1999).
[30]J. E. Hahn, R. A. Scott, K. O. Hodgson, S. Doniach, S. R. Desjardins, and E. I. Solomon, Chem. Phys. Lett. **88**, 595 (1982).
[31]M. Belli, A. Scafati, A. Bianconi, S. Mobilio, L. Palladino, A. Reale, and E. Burattini, Solid State Commun. **35**, 355 (1980); A. Manceau, A. I. Gorshkov, and V. A. Drits, Am. Mineral. **77**, 1133 (1992).
[32]C. R. Horne, U. Bergmann, M. M. Grush, R. C. C. Perera, D. L. Ederer, T. A. Callcott, F. J. Cairns, and S. P. Cramer, J. Phys. Chem. B **104**, 9587 (2000).
[33]M. Pouchard, A. Villesuzanne, and J.-P. Doumerec, J. Solid State Chem. **162**, 282 (2001).
[34]M. G. Kim, Y. S. Im, E. J. Oh, K. H. Kim, and C. H. Yo, Physica B **229**, 338 (1997).
[35]A. Chainani, M. Mathew, and D. D. Sarma, Phys. Rev. B **46**, 9976 (1992).
[36]Y. Iwasawa, *X-Ray Absorption Fine Structure for Catalyst and Surfaces* (World Scientific, Singapore, 1996).
[37]G. J. Colpas, M. J. Maroney, C. Bagyinka, M. Kumar, W. S. Willis, S. L. Suib, N. Baidya, and P. K. Mascharak, Inorg. Chem. **30**, 920 (1991).
[38]A. Bianconi, in *X-Ray Absorption: Principles, Applications, Techniques of EXAFS, SEXAFS, and XANES*, edited by D. C. Koningsberger (Wiley, New York, 1988).
[39]J. A. Victoreen, J. Appl. Phys. **19**, 855 (1948).
[40]D. C. Koningsberger and R. Prins, in *X-Ray Absorption: Principles, Applications, Techniques of EXAFS, SEXAFS, and XANES* (Wiley, New York, 1988).
[41]I. Nakai and T. Nakagome, Electrochem. Solid-State Lett. **1**, 259 (1998).
[42]I. Nakai, K. Takahashi, Y. Shiraishi, T. Nakagome, F. Izumi, Y. Ishii, F. Nishikawa, and T. Konishi, J. Power Sources **68**, 536 (1997).
[43]A. Rougier, C. Delmas, and A. V. Chadwick, Solid State Commun. **94**, 123 (1995).
[44]I. Nakai, K. Takahashi, Y. Shiraishi, T. Nakagome, and F. Nishikawa, J. Solid State Chem. **140**, 145 (1998).
[45]R. D. Shannon, Acta Crystallogr., Sect. A: Cryst. Phys., Diffr., Theor. Gen. Crystallogr. **A32**, 751 (1976).
[46]A. N. Mansour, J. McBreen, and C. A. Melendres, J. Electrochem. Soc. **146**, 2799 (1999).
[47]W. E. O'Grady, K. I. Pandya, K. E. Swider, and D. A. Corrigan, J. Electrochem. Soc. **143**, 1613 (1996).
[48]J.-M. Kim and H.-T. Chung, Electrochim. Acta **49**, 3573 (2004).